Chandra Evidence for Extended X-ray Structure in RY Tau

Skinner, Stephen L.; Audard, Marc; Güdel, Manuel

How to cite

SKINNER, Stephen L., AUDARD, Marc, GÜDEL, Manuel. *Chandra* Evidence for Extended X-ray Structure in RY Tau. In: The Astrophysical journal, 2011, vol. 737, n° 1, p. 19. doi: 10.1088/0004-637x/737/1/19

This publication URL: https://archive-ouverte.unige.ch/unige:185555
Publication DOI: 10.1088/0004-637x/737/1/19

To appear in the Astrophysical Journal

Chandra Evidence for Extended X-ray Structure in RY Tau

Stephen L. Skinner[1], Marc Audard[2], and Manuel Güdel[3]

ABSTRACT

We report results of a sensitive *Chandra* ACIS-S observation of the classical T Tauri star RY Tau. Previous studies have shown that it drives a spectacular bipolar jet whose blueshifted component is traced optically along P.A. $\approx 295^\circ$ at separations of $1.''5$ - $31''$ from the star. Complex X-ray emission is revealed, including a very soft non-variable spectral component (some of which may originate in shocks), a superhot flaring component (T $\gtrsim$ 100 MK), and faint extended structure near the star. The structure is visible in deconvolved images and extends northwestward out to a separation of $1.''7$, overlapping the inner part of the optical jet. Image analysis suggests that most of the extension is real, but some contamination by PSF-induced structure within the central arcsecond may be present. The predicted temperature for a shock-heated jet based on jet speed and shock speed estimates from optical measurements is too low to explain the extended X-ray structure. Either higher speed material within the jet has escaped optical detection or other mechanisms besides shock-heating are involved. Alternative mechanisms that could produce higher temperature plasma at small offsets to the northwest of RY Tau include magnetic heating in the jet, hot plasmoids ejected at high speeds, or X-ray emission from a putative close companion whose presence has been inferred from *Hipparcos* variations.

Subject headings: stars: individual (RY Tau) — ISM: Herbig-Haro objects — stars: pre-main sequence — stars: winds, outflows — X-rays: stars

[1]Center for Astrophysics and Space Astronomy (CASA), Univ. of Colorado, Boulder, CO, USA 80309-0389; stephen.skinner@colorado.edu

[2]ISDC Data Center for Astrophysics, University of Geneva, Ch. d'Ecogia 16, CH-1290 Versoix, Switzerland and Geneva Observatory, University of Geneva, Ch. des Maillettes 51, CH-1290 Versoix, Switzerland; marc.audard@unige.ch

[3]Dept. of Astronomy, Univ. of Vienna, Türkenschanzstr. 17, A-1180 Vienna, Austria; manuel.guedel@univie.ac.at

1. Introduction

Jets are known to be associated with a diverse range of astronomical objects including active galactic nuclei, compact binaries, planetary nebulae, brown dwarfs, and young stellar objects (YSOs). The mechanisms responsible for jet launching, collimation, and heating are still not well-understood so astrophysical jets continue to be the focus of numerous observational, laboratory, and theoretical studies.

Jets are thought to be intimately linked to the process of accretion. In star-forming regions, collimated jets have been detected from accreting YSOs such as embedded protostars, classical T Tauri stars (TTS), and Herbig Ae/Be stars. Jets from YSOs are capable of influencing the star-formation process by injecting energy, momentum, and associated turbulence into the surrounding molecular cloud. Spectroscopic studies suggest that some YSO jets are rotating (Chrysostomou et al. 2008), implying that jets play a role in transporting angular momentum outward in young star-disk systems. Precessing jets also provide an indirect means of detecting dynamical interactions in close protostellar binaries (Su et al. 2007).

YSO jets have traditionally been identified and studied using high-resolution optical, near-IR, or radio telescopes. But, the improvement in angular resolution afforded by current-generation X-ray telescopes has revealed that YSO jets are also capable of emitting soft X-rays originating in plasma at temperatures of a few MK. X-ray observations are important because they provide information on physical conditions in the hottest jet plasma that is not accessible at optical or infrared wavelengths. Only a few examples of X-ray emitting YSO jets are known so far. The most striking example is the classical TTS DG Tau, which shows soft X-ray emission extending outward along the optical jet axis to a distance of $\approx 5''$ from the star (Güdel et al. 2005, 2008). We report here the first evidence of asymmetric X-ray structure in the accreting TTS RY Tau that is visible as faint extension toward the northwest. The extended structure may be associated with the inner region of its optically-traced jet, but alternative interpretations are also discussed.

2. RY Tau

RY Tau is a classical TTS lying in the Taurus dark cloud (d = 134 pc; Bertout, Robichon, & Arenou 1999). It is highly variable in the optical and its spectral type is somewhat uncertain (Holtzman, Herbst, & Booth 1986). Its mass is at the high end of the range for TTS. Recent work suggests a spectral type of F8 III - G1-2 IV, mass $M_* = 1.7$ - $2.0\ M_\odot$, luminosity $L_* = 12.8\ L_\odot$, and $A_V = 2.2 \pm 0.2$ mag (Schegerer et al. 2008 and references therein). The star rotates rapidly with $v\sin i = 52 \pm 2$ km s^{-1} (Petrov et al. 1999). Previous

optical and IR studies have shown that RY Tau has an accretion disk and is accreting at a rate $\dot{M}_{acc} = 6\ (\pm 3) \times 10^{-8}\ M_\odot\ yr^{-1}$ (Schegerer et al. 2008; Angra-Amboage et al. 2009, hereafter AA09). The accretion is accompanied by mass-loss in the form of a spectacular bipolar jet known as HH 938 (St.-Onge & Bastien 2008, hereafter SB08) and a wind (Gómez de Castro & Verdugo 2007). Hα images show several jet knots extending outward to a separation of 31″ from the star along P.A. $\approx 295°$ (measured east from north), and traced inward to a separation of $\approx$1.″5 (SB08). YSO jets traced so close to the star are rare. The fainter counterjet is optically visible in the opposite direction out to 3.′5 from the star.

RY Tau is suspected to be a binary on the basis of nonuniform photocenter motions in *Hipparcos* observations. Analysis of the *Hipparcos* variations initially gave a direction P.A. = 316.6° ± 37.6° toward the putative companion, but a later reanalysis found P.A. = 304° ± 34° and a companion separation $\geq$23.6 mas (Bertout et al. 1999). But, no companion has yet been found (Leinert et al. 1993; Schegerer et al. 2008; Pott et al. 2010). The P.A. of the putative companion is close to that of the optical jet and it has been suggested that the jet may have been responsible for the *Hipparcos* variations (AA09).

A previous *Chandra* ACIS-S/HETG observation of the TTS HDE 283572 (ObsId 3756) captured RY Tau as a bright off-axis X-ray source (Audard et al. 2005), but the archived data cannot be used to search for jet emission close to the star because of off-axis image distortion. This motivated us to obtain a higher-quality *Chandra* image with RY Tau placed on-axis.

3. Chandra Observation

The *Chandra* observation (ObsId 10991) occurred on 2009 December 31 from 05:31 - 22:15 TT. The exposure live time was 55,766 s. Exposures were obtained using the ACIS-S (Advanced CCD Imaging Spectrometer) array in faint timed-event mode. ACIS-S was restricted to the standard 1/4 subarray with only one chip (S3) enabled. This reduces the field-of-view to 2.1′ × 8.4′ but allows a shorter 0.8 s frame readout time (compared to 3.2 s for the full ACIS-S array), thus mitigating photon pileup[4] for this bright source (Sec. 4.2). RY Tau was placed at the nominal ACIS-S 1/4 subarray aimpoint.

[4]Pileup occurs when two or more photons are detected as a single event. Severe pileup can broaden the source image and artificially harden the X-ray spectrum. For more details, see:: http://cxc.harvard.edu/ciao/why/pileup_intro.html .

The data were analyzed using standard science threads in CIAO[5] version 4.1.2 and calibration data from CALDB version 4.1.4. The default ACIS pixel randomization applied during standard processing slightly broadens the point-spread-function (PSF) and was removed for image analysis. However, we have compared our imaging results (Sec. 4.3) with the default pixel randomization retained and there are no significant differences. CIAO *specextract* was used to extract source and background spectra (background is negligible). The tool *acisreadcorr* was used to remove a readout streak running east-west through the source along P.A. = 91°/271°. Spectral fitting was undertaken with XSPEC vers. 12.4.0 [6].

4. Results

4.1. The X-ray Field Near RY Tau

Figure 1 shows the *Chandra* broad-band image in the vicinity of RY Tau. The bright emission from RY Tau dominates the field, but 5 fainter sources within ≈1′ of it were found by the CIAO wavelet detection tool *wavdetect*. Their properties are summarized in Table 1. No optical or near-IR counterparts were found for any of these field sources in the *HST* Guide Star Catalog (GSC) or 2MASS catalog.

A direct comparison of the X-ray source positions (R.A., Dec.) in Table 1 with the optical knot positions in SB08 cannot be made because the tabulated SB08 optical positions have large systematic errors. Specifically, we note that the reference position of RY Tau given in Tables 1 and 2 of SB08 is offset 7.″0 eastward and 0.″5 northward from its *HST* GSC v. 2.3.2 position (= *HST* J042157.41+282635.48). However, a comparison of the optical knot offsets relative to the star given by SB08 with the *Chandra* source offsets (Table 1) reveals a possible match between *Chandra* source no. 2 and optical knot Ha6. The offset of X-ray source no. 2 (CXO J042155.93+282647.55) from the RY Tau X-ray centroid is 23.″1, and its offset relative to the *HST* GSC position of RY Tau is 22.″9. These values are close to the 22.″2 offset of knot Ha6 from the reference position of RY Tau listed in Table 2 of SB08, but this comparison does not take into account any proper motion that might have occurred in knot Ha6 since the SB08 observation on 25 February 2005. The offset of X-ray source no. 2 from the RY Tau X-ray peak is along P.A. = 302° which is comparable to the value P.A. = 293° computed for the Ha6 optical knot direction (Table 2 of SB08). Also of potential

[5]Further information on *Chandra* Interactive Analysis of Observations (CIAO) software can be found at http://asc.harvard.edu/ciao .

[6]http://heasarc.gsfc.nasa.gov/docs/xanadu/xanadu.html.

interest is the fainter X-ray source no. 4 (CXO J042200.09+282613.39), which lies exactly in the opposite direction along P.A. = 122°. Since X-ray sources no. 2 and no. 4 have relatively high median photon energies (Table 1), deep follow-up optical observations will be needed to determine whether they are chance superpositions of foreground or background objects near the jet axis, or shocked features in the jet.

4.2. X-ray Variability and Pileup Estimates

The 0.2 - 8 keV broad-band light curve of RY Tau (Fig. 2-top) is clearly variable, showing an increase in count rate by a factor of ∼2 during the first 10 ks, followed by a slow decay with an e-folding timescale $\tau \approx 10$ ks. The variability is associated with the harder emission above ≈1 keV and is likely due to magnetic activity. If we consider only the softest emission in the 0.2 - 1.0 keV range (910 events) where shock emission could contribute significantly, little or no variability is found (Fig. 2-bottom). Specifically, the Bayesian-method CIAO tool *glvary* (Gregory & Loredo 1992, 1996) gives a variability probability $P_{var} = 0.05$ (0.2 - 1.0 keV). But, if the energy range is increased to 0.2 - 1.5 keV, *glvary* gives $P_{var} = 0.999$, so the emission above 1 keV is definitely variable.

Even though a flare occurred, we were fortunate to avoid any severe pileup as a result of the judicious use of a 1/4 ACIS-S subarray and its shorter 0.8 s frame readout time. We estimated the pileup fraction using the CIAO *pileup_map* tool and the *PIMMS*[7] simulator. Moderate pileup of ≈10% - 13% occurred during the flare-peak interval (elapsed time $t = 7$ - 13 ks) but pileup was negligible at ≤5% after the flare had decayed ($t > 25$ ks). Since the pileup was moderate and only present over a short ∼6 ks time interval spanning about 10% of the exposure time, it did not adversely affect the data. The telltale "donut hole" source image characteristic of severe pileup was not seen and any pileup-induced broadening of the source image amounted to no more than a few percent (Sec. 4.3.5). Nevertheless, we have exercised considerable caution in our image and spectral analysis to insure that our results are not affected by the moderate pileup.

[7]http://asc.harvard.edu/toolkit/pimms.jsp

4.3. RY Tau Images and Extended X-ray Structure

4.3.1. X-ray Positions

The broad-band (0.2 - 8 keV) X-ray centroid position of RY Tau measured with the HEASOFT XIMAGE *centroid* [8] tool using source counts centered inside a box of half-width 3″ is J042157.41+282635.24. This result is unchanged if the box half-width is reduced to 1.″5. The CIAO *dmstat* tool gives an identical centroid position. The X-ray centroid is offset 0.″24 south of the *HST* GSC vers. 2.3.2 position of RY Tau and 0.″33 southwest of the 2MASS position (Table 1 notes; Fig. 3). These small offsets are within *Chandra*'s ACIS-S absolute astrometric accuracy of ≈0.″42 (90% confidence) for on-axis sources[9].

Since the flare resulted in a flux increase at higher energies above 2 keV (Sec. 4.4) we compared X-ray centroids in soft (0.2 - 2 keV) and hard-band (2 - 8 keV) images. Any significant offset would obviously be of interest since it could signal a second star in the system. To avoid any possible effects of pileup, we measured the positions using events recorded during the initial flare rise segment (t = 0 - 7 ks) and the post-flare segment ($t >$ 25 ks). A small offset is seen in both time segments but it is of low significance. Specifically, the hard-band centroid is offset to the northwest of the soft-band centroid by ≈0.″03 - 0.″05 along P.A. ≈300° - 320°. The larger offset corresponds to the flare rise phase. Although the offset is too small to be considered statistically significant, the P.A. is consistent with that of the putative *Hipparcos* companion (Sec. 2) and again raises the question of whether a second object might be present.

4.3.2. Azimuthal Count Distribution

Evidence for X-ray extension toward the northwest is seen when extracting counts within non-intersecting regions of equal angular and radial size distributed along different directions from the X-ray source. The wedge-shaped regions used for this count extraction subtend an angular width of 10° and are restricted to radii within the range $1'' \leq r \leq 3''$ from the X-ray peak. As Figure 3 shows, a significant excess in soft-band counts (0.2 - 2 keV) is present along the optical jet axis at P.A. ≈ 295° and also at higher P.A. ≈ 310° - 330°. The excess is present in images based on the full exposure and in images restricted to post-flare data only ($t >$ 25 ks). It is also present along P.A. ≈ 305° - 325° in images with sub-pixel

[8]http://heasarc.gsfc.nasa.gov/docs/xanadu/ximage/ximage.html

[9]http://asc.harvard.edu/proposer/POG/

event repositioning (SER)[10] applied. No significant excess was found in any of the other three quadrants. A similar analysis based on medium-energy 2 - 4 keV images shows a weak excess toward the northwest, but it is of low statistical significance and its morphology is not stable as a function of the number of iterations in deconvolved images (Sec. 4.3.4). Thus, a deeper exposure will be needed to determine whether any significant excess is present at energies above 2 keV.

4.3.3. PSF Asymmetry

The regions used to extract the source counts plotted in Figure 3 exclude counts at small offsets of $r < 1''$. This precaution was necessary because a recently-discovered asymmetry in the *Chandra* PSF can produce artificial structure at radii $0.''6 < r < 1''$ over a limited range of position angles P.A.$_{asymm}$ = 195° − ROLL (±25°). For the RY Tau observation, the nominal roll angle was ROLL = 268.6° so P.A.$_{asymm}$ = 286.4° (±25°). The region that may be affected by the PSF asymmetry is plotted in Figure 4. The asymmetry produces hook-shaped artificial structure within the central arcsecond in *Chandra* HRC images and there is evidence that the asymmetry is also present in ACIS data. There is no indication that the asymmetry affects image structure at radii $r > 1''$. The asymmetry was reported in October 2010 after the RY Tau observation was obtained [11].

4.3.4. Image Deconvolution

Since the initial image analysis (Sec. 4.3.2) suggested that extension toward the northwest is present in the soft-band, we constructed several different deconvolved images using CIAO *arestore*, which is based on the Lucy-Richardson method (Lucy 1974; Richardson 1972). This procedure removes some of the blurring effect on the source image due to the telescope optics. We obtained deconvolved images in several different energy bands but focus here on images in the soft 0.2 - 2 keV band. We compared deconvolved images generated using events from the full exposure with those using only events from the low-pileup post-flare segment. The deconvolution used observation-specific energy-filtered PSF image files created using the *Chart* and *MARX* simulators according to CIAO science thread procedures. These

[10]http://cxc.harvard.edu/ciao/why/acissubpix.html

[11]Current information on the PSF asymmetry can be found at:
http://cxc.harvard.edu/ciao/caveats/psf_artifact.html

PSF images take into account the source spectrum during the time interval of interest and the source position on the CCD relative to the optical axis.

Extended structure toward the northwest is clearly seen in deconolved images in the 0.2 - 2 keV band. The extension is present in deconvolved images generated with and without pixel randomization, and is visible in both full-exposure and post-flare ($t > 25$ ks) images. Figure 4 shows the raw 0.2 - 2 keV image before deconvolution, along with deconvolved images for the full-exposure and post-flare time interval. For comparison, deconvolved images using 50 and 100 iterations in *arestore* are shown.

The morphology of the extended structure in all of the soft-band deconovolved images in Figure 4 is quite similar. Overall, the extended structure is fainter in the post-flare images since they are based on only about half the number of soft-band counts as the full-exposure images. Also, some variation is expected since the PSF used in the deconvolution is spectrum-dependent and the source spectrum was softer during the post-flare segment (Sec. 4.4). As can be seen, increasing the number of iterations from 50 to 100 causes some of the fainter extension to disappear and the "bridge" connecting the extended structure to the star becomes more tenuous. Although some clumpiness is present in the extended emission, this should not be construed as real physical substructure. Some clumpiness is expected in 0.″125 subpixel images without randomization (as compared to the physical pixel size of 0.″492) and because of PSF substructure [12]. The deconvolved images in Figure 4 are based on input images without pixel randomization. If pixel randomization is retained, the extended structure is similar, but slightly broader. This is to be expected since randomization broadens the source image on the CCD.

As Figure 4 shows, there is some overlap of the extended X-ray emission with the region where the known PSF asymmetry can produce artificial structure. Thus, some of the extended structure within 1″ of the star may be PSF-induced. But, it is clear from the figure that there is considerable extended structure outside of the region affected by the PSF asymmetry. Specifically, the full-exposure soft-band deconvolved image contains 60 counts at $r > 0.''6$, half of which lie outside the PSF asymmetry region. The observed structure extends outward to at least 1.″7 from the X-ray peak, well beyond the limit $r = 1''$ where the PSF asymmetry can affect the image. Furthermore, the extended emission does not display the characteristic hook-like shape induced by the PSF asymmetry. We thus conclude that most of the extended structure is real, but some contamination from the PSF asymmetry may be present at radii $r < 1''$ near P.A. = 286°.

The extended X-ray structure in the soft-band deconvolved images is visible across a

[12] http://cxc.cfa.harvard.edu/cal/Hrma/users_guide/hrma-notes.pdf

range of position angles P.A. ≈ 285° - 325°. A linear fit which takes the distribution of counts across this P.A. range into account gives a best-fit direction P.A. = 305° for the extension axis, measured relative to the soft-band X-ray centroid. The extension is visible outward to a separation of ≈1.″7 (≈228 AU) and inward to a separation of ≈0.″6 (≈80 AU). The extended structure partially overlaps the inner region of the optical jet (Fig. 4). The innermost Hα jet knot designated HaA by SB08 lies at an offset of 1.″5 from the star along P.A. = 299°, and the knot detected in [O I] by AA09 lies at an offset of 1.″35 along P.A. = 294°. But, as Figure 4 shows, the soft-band X-ray extension is less-collimated than the optical jet and extends to higher P.A. values. The best-fit soft-band X-ray extension axis at P.A. = 305° is in good agreement with the value inferred for the direction of the putative companion from *Hipparcos* variations (Sec. 2). It is thus not clear that all of the wide X-ray extension is associated with the more tightly collimated optical jet.

4.3.5. Checks for Flare-Induced PSF Effects

Photon pileup can artificially broaden the PSF [13]. As mentioned above (Sec. 4.2), moderate pileup of 10% - 13% occurred during the flare peak time interval, It is thus important to note that the extended X-ray structure is still present in deconvolved images based on low-pileup post-flare data (Fig. 4). This provides added confidence that the X-ray extension is not due to pileup-induced PSF broadening.

We checked for source broadening by applying Gaussian fits to the source image during the flare-peak time interval (t = 7 - 13 ks) and the post-flare phase ($t >$ 25 ks). The source profile was fitted separately in the north-south and east-west directions. No energy filtering was applied. We found no evidence of broadening of the source FWHM during the flare at levels above ≈3%.

As a further check for changes in the source size during the flare, we plotted the event positions in (X,Y) sky-pixel coordinates as a function of time (Fig. 5). The (X,Y) values correspond to (R.A., Dec.) but are in units of pixel coordinates. As Figure 5 shows, there is more scatter in (X,Y) during the flare than afterward. Using (X,Y) data binned at 5 ks intervals, we find that the standard deviation of the mean (X,Y) positions for each bin is about 3% - 6% larger during the flare than afterword. This is comparable to, but slightly larger than that inferred above from Gaussian fits. Some of this difference is likely due to a low-level of flare-induced PSF broadening but a flaring close companion could also cause

[13] An example of pileup-induced source broadening due to a flare can be found at: http://cxc.cfa.harvard.edu/cal/ASPECT/psf_degrade/

positional scatter.

4.4. The X-ray Spectrum

The ACIS-S CCD spectrum shown in Figure 6 was extracted from a circular region of radius 3″ centered on the star and thus includes emission from both the star and the extended X-ray structure. No spectrum of the jet-like feature itself was obtained due to its faintness and proximity to the bright stellar source. Several emission lines, or line blends, are visible in the spectrum. These lines reflect a broad range of X-ray temperatures. Cool plasma is revealed by the O VII He-like triplet (E_{lab} = 0.57 keV) which forms at a characteristic temperature T $\sim$ 2 MK and the Ne IX triplet (E_{lab} = 0.92 keV) which forms at T $\sim$ 4 MK. At the other extreme, we also detect the Fe Kα complex which forms in very hot plasma at T $\sim$ 40 MK.

We extracted separate spectra for the flare rise (t = 0 - 7 ks; 2350 counts), flare decay (t = 13 - 30 ks; 3848 counts), and late post-flare (t = 30 - 58.6 ks; 4011 counts) segments. The above segments excluded the time interval t = 7 - 13 ks near flare peak during which photon pileup reached its maximum of $\approx$10% - 13% and could result in some artificial hardening of the energy spectrum. Each spectrum was fitted with an absorbed two-temperature (2T) *vapec* optically thin plasma model consisting of a cool (kT_1) and hot (kT_2) component. Extremely hot plasma at a temperature $kT_{2,flare} \gtrsim$ 9 keV (T $\gtrsim$ 100 MK) was present during the flare rise and decay segments, and the Fe Kα line complex was strongest during the flare rise segment (Fig. 6-middle). During the post-flare segment, the temperature of the hot plasma component had decreased by a factor of $\sim$2 and the count rate was more stable. But, high-temperature lines are still present in the post-flare spectrum including faint Fe Kα emission and strong emission from the Si XIII He-like triplet at 1.86 keV. The late post-flare spectrum has negligible pileup (<5%) and its best-fit parameters are given in Table 2. They are similar to values found for other TTS. The best-fit absorption $N_H = 5.5\ [4.7 - 6.8] \times 10^{21}$ cm^{-2} equates to A_V = 2.5 [2.1 - 3.1] mag (Gorenstein 1975 conversion) which is consistent with the optical value $A_V = 2.2 \pm 0.2$ mag (Calvet et al. 2004). The unabsorbed X-ray luminosity during the post-flare segment was log L_X(0.2 - 10 keV) = 30.7 ergs s^{-1}, but was at least 0.7 dex larger during the flare.

Although the 2T *vapec* model generally produces an acceptable fit of the post-flare spectrum, it underestimates the flux in the weak emission feature near 0.57 keV that is likely the O VII He-like triplet (Fig. 6-bottom). This flux deficit is still present even if the O abundance is allowed to vary in the fit. This suggests that the O VII line may be of nonstellar origin, arising in very cool plasma in the jet or an accretion shock. Adding a

Gaussian component to the 2T *vapec* model at a fixed width FWHM = 110 eV corresponding to ACIS-S spectral resolution improves the fit slightly and gives an unabsorbed continuum-subtracted line flux $F_{X,OVII} = 4.7 \times 10^{-15}$ ergs cm^{-2} s^{-1}.

5. Discussion

5.1. X-ray Emission from the Jet?

The extended structure shown in Figure 4 overlaps the inner region of the optical jet. This raises the interesting possibility that the extended X-ray emission arises in the jet, close to the star. But, as discussed below, there are legitimate questions as to whether the RY Tau jet speed and shock speed are sufficient to produce soft-band thermal X-rays by shock-heating alone.

The predicted temperature for a shock-heated jet with a shock speed v_s is (Raga et al. 2002):

$$T_s = 1.5 \times 10^5 \left[\frac{v_s}{100 \text{ km s}^{-1}}\right]^2 \ K. \tag{1}$$

Assuming the jet impacts a stationary target ($v_s \approx v_{jet} \approx 165$ km s^{-1}), then the maximum shock temperature is $T_s \approx 0.4$ MK (k$T_s \approx 0.035$ keV). This temperature is a factor of $\sim$3 lower than that needed to produce detectable thermal X-ray emission at kT $\approx$ 0.1 - 0.2 keV (T $\approx$ 1 - 2 MK), below which *Chandra* has little sensitivity. The detection of soft-band X-rays from the jet thus seems to require either a higher jet speed (and shock speed) than assumed above, or an additional heating mechanism other than shocks. The deprojected terminal speed of the jet is uncertain by a factor of $\sim$2 (AA09). Doubling the shock speed in the above calculation to $v_s = 330$ km s^{-1} would increase the shock temperature to $T_s \approx 1.6$ MK (k$T_s \approx 0.14$ keV), which is high enough to produce soft X-ray emission. But, a shock speed of $v_s = v_{jet} \approx 330$ km s^{-1} is at odds with optical data, which suggest a *lower* shock speed in the range $v_s \approx$ 20 - 50 km s^{-1} (AA09). Unless very high velocity jet plasma has escaped optical detection, it is not obvious that the jet speed is sufficient to produce shock-heated plasma at the X-ray temperatures sufficient for detection in the *Chandra* soft band.

If the soft-band extended X-ray emission detected by *Chandra* is due to the jet, then the above estimates suggest that other mechanisms besides shocks are needed to heat the

jet to X-ray emitting temperatures. In this regard, magnetic fields may play a role. Recent observations have in fact given strong support for the presence of magnetic fields in YSO jets. A notable discovery is the detection of linearly polarized radio emission in the HH 80-81 jet (Carrasco-González et al. 2010). Linearly polarized radio emission is typical of synchrotron radiation and is produced by relativistic particles trapped in a magnetic field threading the HH 80-81 jet. The new results for HH 80-81 raise the interesting question of whether the RY Tau jet might also show signs of nonthermal radio emission that could signal an entrained magnetic field.

Even if the jet is contributing to the extended soft-band X-ray emission, its contribution to the total X-ray luminosity of RY Tau is predicted to be very low. The predicted intrinsic (unabsorbed) luminosity of the shocked jet is the lesser of the two values corresponding to radiative and non-radiative cases (eqs. 8 and 9 of Raga et al. 2002). For the range of parameters relevant to RY Tau, the minimum corresponds to the radiative shock case:

$$L_{r,jet} = 4.1 \times 10^{-6} \frac{n_o}{100 \text{ cm}^{-3}} \left[\frac{r_{bs}}{10^{16} \text{ cm}}\right]^2 \left[\frac{v_s}{100 \text{ km s}^{-1}}\right]^{5.5} L_\odot \qquad (2)$$

where n_o is the preshock number density, r_{bs} is the characteristic radius of the bow shock around its axis, and v_s is the shock speed. For purposes of an estimate, we adopt the following values used by AA09. The electron density in the RY Tau jet is not well-determined but is assumed to be similar to that of other YSO jets studied at high angular resolution with a value that decreases with radius from the star $n_o = 5000(1''/r)$ cm^{-3} ($r \geq 0.''5$). For the range of offsets at which the X-ray extension is visible (Fig. 3), the value $n_o = 5000$ cm^{-3} at $r = 1''$ is a reasonable estimate. The optical jet full-width is nearly constant as a function of distance from the star (AA09) and we adopt a full-width of $0.''3$, which equates to a jet radius $r_{bs} = 20$ AU $= 3 \times 10^{14}$ cm (d = 134 pc). Assuming a shock speed $v_s = v_{jet}$ = 165 km s^{-1} (SB08) gives $L_{r,jet} = 1.1 \times 10^{28}$ ergs s^{-1}. It is obvious from equation (2) that the above estimate is quite sensitive to the assumed shock speed v_s.

Could soft X-ray emission from a shocked jet of the above luminosity $L_{r,jet} = 1.1 \times 10^{28}$ ergs s^{-1} generate sufficient counts to explain the extended X-ray structure? To address this question, we assume that the jet has a simple thermal spectrum with a characteristic shock temperature kT$_s$ = 0.035 keV corresponding to $v_s = v_{jet}$ = 165 km s^{-1} (eq. 1). The absorption column density toward the extended jet-like structure is not directly known from observations, but since the structure is offset from the star we assume an extinction toward the jet of A$_V$ = 1 mag, or about half the stellar value (Sec. 2). This extinction corresponds to an absorption column density N$_H$ = 1.6×10^{21} cm^{-1} (Vuong et al. 2003). Using this simple model and an unabsorbed flux density F$_{X,unabsorbed}$ = 5.1×10^{-15} ergs cm^{-2} s^{-1} corresponding to the above value of $L_{r,jet}$ (d = 134 pc), the *Chandra* PIMMS simulator predicts that <1

count will be detected in the 0.2 - 2 keV range in a 56 ks ACIS-S exposure. By comparison, the extended structure in the soft-band deconvolved image contains 30 counts, excluding those inside the PSF asymmetry region (Sec. 4.3.4).

In order to attribute the 30 soft-band extended counts lying outside the PSF asymmetry region to a shocked jet, a higher jet luminosity $L_{r,jet} \approx 1.2 \times 10^{29}$ ergs s^{-1} is needed. This value is one-seventh of the soft-band luminosity (star + extension) of $L_{X,1} = 8.4 \times 10^{29}$ ergs s^{-1} determined from spectral fits (Table 2). To achieve this higher jet luminosity, the values of one or more of the three jet parameters in equation (2) would need to be increased. If the values of n_0 and r_{bs} are held fixed to those used above, then a higher shock speed $v_s \approx 254$ km s^{-1} ($kT_s \approx 0.084$ keV) would be required. Although this shock speed is plausible given that the deprojected jet speed is uncertain by a factor of $\sim$2, it is at least five times greater than shock speeds inferred from optical data (AA09).

5.2. Plasmoid Ejections?

As shown above, it is difficult to account for shock-induced X-ray emission in the jet based on the optically-determined values $v_{jet} = 165$ km s^{-1} and shock speeds $v_s < 100$ km s^{-1}. If the extended soft-band X-ray emission originates in the jet, then either higher speeds are needed or other jet heating mechanisms besides shocks are required.

Plasmoid ejections provide one possible means of attaining higher speeds and sufficiently high plasma temperatures to produce X-ray emission The model developed by Hayashi et al. (1996) predicts that hot plasmoids ($T_p \sim 10^7$ - 10^8 K) will be ejected at high speeds in bipolar directions during hard protostellar X-ray flares. As the plasmoids move outward and cool, they may be revealed optically as inhomogeneities within the jet. The plasmoid ejection speed is predicted to be $v_p \sim (2 - 5) \times v_K$, where $v_K = \sqrt{GM_*/R_{in}}$ is the Keplerian rotation speed at the inner edge of the disk. For RY Tau ($R_{in} = 0.3$ AU, $M_* = 1.7$ $M_\odot$; Schegerer et al. 2008) we obtain $v_K = 71$ km s^{-1} and plasmoid speeds $v_p \sim 140$ - 350 km s^{-1}. Hot ejected plasmoids moving outward at speeds of several hundred km s^{-1} through the stellar or disk wind, or plowing into accreting gas, would be capable of producing soft X-rays from shocks. Specifically, adopting $v_s = 350$ km s^{-1} gives $T_s = 1.8$ MK or $kT_s = 0.16$ keV) (eq. 1), which lies near the low end of the temperature range detectable by *Chandra* ACIS-S.

In order for hot plasmoids to escape, they would need to be ejected at (or accelerated to) speeds in excess of the escape speed. At the surface of RY Tau, the escape speed is v_{esc} = 410 km s^{-1}, assuming $M_* = 1.7$ $M_\odot$ and $R_* = 3.85$ $R_\odot$ (Schegerer et al. 2008). This value

of v_{esc} is slightly above the maximum predicted plasmoid ejection speed in the Hayashi et al. model. But, the plasmoids are expected to form in the flaring region above the stellar surface where the escape speed will be less. A plasmoid that has escaped at an ejection speed $v_p \sim 350$ km s^{-1} would traverse a projected distance equivalent to 1″ in 1.8 years at the distance to RY Tau. However, this assumed speed could be an underestimate given that coronal mass ejections (CMEs) from the Sun can reach speeds of ≥1000 km s^{-1} (Aarnio et al. 2011; Gopalswamy et al. 2005). The Hayashi et al. model predicts that a cold dense disk wind will form. Ejected plasmoids moving outward would create disturbances or shocks in the disk wind (or the stellar wind). By analogy, interactions of CMEs with the solar wind are indeed known to occur and can produce shocks and wind disturbances (Gosling et al. 1995; Wang et al. 2001). Plasmoids that fail to reach escape speed could also shock against the outflowing wind on reentry. Variations on the plasmoid model have been proposed to explain hot X-ray plasma detected near OB stars (Howk et al. 2000; Waldron & Cassinelli 2009).

The above discussion focuses on shock emission at temperatures of a few MK that could be produced by high-speed plasmoids. But, if the plasmoids have temperatures $T_p \sim 10^7$ - 10^8 K then they could themselves be sources of harder X-rays ($kT_p \sim 1$ - 8 keV), independent of any soft shock-induced emission. As a representative case, we consider an ejected plasmoid of temperature $T_p \sim 10^7$ - 10^8 K and number density n_p. The radiative cooling time of the plasmoid is $\tau_{rad} = 3kT_p/n_p\Lambda(T_p)$, where $\Lambda(T)$ is the plasma emissivity per unit emission measure. As Figure 10 of Audard et al. (2004) shows, the solar-abundance value of $\Lambda(T)$ over the temperature range 10^7 - 10^8 K is nearly constant with an average value $\Lambda \sim 2.5 \times 10^{-23}$ ergs cm^3 s^{-1}. Using this average value for Λ, the radiative cooling time becomes $\tau_{rad} \sim (5 - 50)/n_{p,6}$ years, where $n_{p,6}$ is the plasmoid density in units of 10^6 cm^{-3}. As noted above, it would take about 2 years for a high-speed plasmoid to move out to a separation of 1″ where the extended X-ray structure is seen. If we require $\tau_{rad} \gtrsim 2$ y then the plasmoid density cannot be much larger than $n_p \sim 10^6$ - 10^7 cm^{-3}.

The above density constraint only takes radiative cooling into account and is thus a very rough estimate. More detailed numerical simulations would be needed to determine how the temperature, density and speed of an ejected plasmoid evolve as it moves away from the T Tauri star and interacts with surrounding material. Such simulations would need to take into account such potentially important factors as adiabatic cooling, the influence of any jet magnetic field on plasmoid expansion, and plasma instabilities. Obviously, the physical picture could be considerably more complicated for a TTS than for the Sun. If it can be demonstrated that hot ejected plasmoids can survive for a few years (or less, if they are moving at the higher speeds observed for some solar CMEs), then a trail of such plasmoids ejected during repetitive flares could be revealed as high-temperature plasma offset from the

star, perhaps explaining the X-ray extension seen in the RY Tau images.

5.3. A Close Companion?

As previously noted (Sec. 4.3.4), the soft-band X-ray extension is centered along an axis toward P.A. $\approx 305°$ from the X-ray peak, but the extension spans a range of $\pm 20°$ in position angle. Interestingly, the central axis direction is nearly identical to that inferred for the putative companion from *Hipparcos* variations (Sec. 2). But, near-IR speckle observations by Leinert et al. (1993) probed the separation range 0.″13 - 13″ and found no companion.

The only objects reported so far at separations similar to the range ≈0.″6 - 1.″7 of the X-ray extension are the Hα knot HaA at a separation of 1.″5 along P.A. = 299° (epoch 2005.15; SB08) and the [O I] (6300 Å) knot at an offset of 1.″35 from the optical centroid along P.A. = 294° (epoch 2002.04; AA09). These knots are believed to be non-stellar shocked structures, and this interpretation is supported by the absence of continuum emission at the [O I] knot position (AA09). The above knot separations were measured in optical observations taken 5 - 8 years prior to our *Chandra* observation and both knots could now have moved outward to separations of >2″ (SB08). In that case, it would seem unlikely that the X-ray extension is related to these knots specifically, but more recently ejected knots could be present at separations of <1.″7 where the X-ray extension is seen.

Given that the near-IR speckle observations of Leinert et al. (1993) found no companion within the offset range 0.″13 - 13″, it would appear that any companion must lie very close to RY Tau. But, searches for a companion at very close separations have also yielded negative results. Keck Interferometer observations at 2 μm found no evidence for a companion within the separation range 2.5 - 30 mas (Pott et al. 2010). The VLTI observations obtained by Schegerer et al. (2008) probed separations down to ∼1 AU (∼75 mas) and neither confirmed nor disproved the existence of the companion inferred from *Hipparcos* data.

When limits on *Chandra*'s spatial resolution are considered, it is apparent that any second X-ray source at a separation of <0.″4 from RY Tau would not be fully resolved. The on-axis ACIS-S PSF core has FWHM = 0.″74 at 1.5 keV, and increases only slightly with energy below 4 keV, but more steeply above 4 keV [14]. This FWHM value is in good agreement with the simulated PSF in Figure 4 which has a half-maximum radius of ≈0.″4, and with the core regions of the soft-band deconvolved images, which are of similar radius. The only indication from the *Chandra* observation that a second object might be present at

[14]http://cxc.cfa.harvard.edu/cal/Hrma/users_guide/hrma-notes.pdf

a separation less than the 0.″13 speckle imaging lower limit is the small ≈0.″03 - 0.″05 offset between the soft and hard X-ray centroids along P.A ≈300° - 320° (Sec. 4.3.1). If two X-ray sources are indeed present then there is some ambiguity as to which one is RY Tau because of the small separation. But, the absorption in the post-flare X-ray spectrum is consistent with that expected for RY Tau (Sec. 4.4), so it is reasonable to assume that the cooler post-flare emission is due to RY Tau. In that case, one would identify the soft-band X-ray peak with RY Tau and the harder peak to the northwest with the (flaring) putative companion. But we caution that the offset between the soft and hard centroids, although suggestive, is of low significance and smaller than what can be reliably measured with *Chandra*. Clearly, any definite proof that a second object is present at a small offset northwest of RY Tau will need to come from higher spatial resolution observations. Infrared or radio interferometry capable of detecting a more heavily-obscured object (possibly a flaring protostar) would seem to offer the most promise.

5.4. Low-Temperature Emission Lines

The origin of the low-temperature O VII and Ne IX emission lines in the RY Tau spectrum is of considerable interest. Although cool plasma in the jet may contribute to this line emission, an accretion shock origin is not yet ruled out. In this regard, we note that these two lines are present even in a spectrum extracted from a small circular region of radius 0.″5 (= 1 ACIS physical pixel) centered on the star. This region lies closer to the star than the extended structure shown in Figure 4. In order to further constrain the origin of these low-temperature lines, X-ray grating spectra which can separate the He-like triplet components and provide electron density information will be required. Such grating spectra have been obtained for the accreting TTS TW Hya and high densities have been inferred from the O VII line, suggesting that it forms in the accretion shock or postshock region (Kastner et al. 2002; Brickhouse et al. 2010).

6. Summary

A sensitive *Chandra* observation of RY Tau reveals complex X-ray emission including a cool steady plasma component, a variable superhot component with a maximum flare temperature T $\gtrsim$ 100 MK, and faint structure extending outward from the star toward the northwest. The flaring hot component is no doubt of magnetic origin but a small (low-significance) offset between the soft and hard X-ray centroids raises the intriguing question of whether the flare occurred on RY Tau or a second object. In contrast, some of the coolest

plasma (including the faint O VII emission line) likely arises in the jet or an accretion shock. Higher resolution X-ray grating spectra will be needed to place tighter constraints on the electron density in the cool plasma in order to distinguish between jet or accretion shocks and any cool coronal component.

Deconvolved soft-band (0.2 - 2 keV) images show faint structure extending outward to a separation of $\approx 1.''7$ from the star. The X-ray extension is visible over a range of position angles spanning P.A. = 285° - 325° with a central axis directed toward P.A. $\approx$ 305°. Most of the extended structure at offsets of $>1''$ is believed to be real, but some artificial extension may be present at smaller offsets of $<1''$ due to a known asymmetry in the *Chandra* PSF directed along P.A. $\approx$ 286° ($\pm$25°).

The extended X-ray structure overlaps the blueshifted optical jet axis at P.A. $\approx$ 295° and some of the X-ray extension could thus be jet-related. But, predicted shock temperatures based on optically-determined jet parameters are lower than required to achieve X-ray temperatures of a few million K. It is possible that the hottest jet material is moving faster than optical data suggest and thereby producing hotter shocked plasma in the jet than might otherwise be expected. Higher-temperature plasma could also be present in the jet if magnetic heating is important. Hot high-velocity plasmoids ejected during repetitive hard X-ray flares could also give rise to extended X-ray emission as a result of their own thermal radiation or by shocking onto intervening material. The plasmoid interpretation is somewhat speculative but is supported by some theoretical YSO flare models and it is well-established that the Sun (a much less active star) commonly launches CMEs at speeds >1000 km s^{-1}. A final possibility is that the X-ray extension is related to a close companion to the northwest of RY Tau whose presence has been inferred from *Hipparcos* variations. However, sensitive ground-based searches for a companion have so far yielded negative results.

This work was supported by *Chandra* award GO0-11028X issued by the Chandra X-ray Observatory Center (CXC). The CXC is operated by the Smithsonian Astrophysical Observatory (SAO) for, and on behalf of, NASA under contract NAS8-03060. MA acknowledges support from Swiss National Science Foundation grants PP002-110504 and PP00P2-130188. We thank V. Kashyap (CXC) for current information on ACIS PSF structure and independent PSF analysis of RY Tau.

REFERENCES

Aarnio, A.N., Stassun, K.G., Hughes, W.J., & McGregor, S.L. 2011, Sol. Phys., 268, 195

Agra-Amboage, V., Dougados, C., Cabrit, S., Garcia, P.J.V., & Ferruit, P. 2009, A&A, 493, 1029 (AA09)

Anders, E., & Grevesse, N. 1989, Geochim. Cosmochim. Acta, 53, 197

Audard, M., Skinner, S.L., Smith, K.W., Güdel, M., & Pallavicini, R. 2005, in Proc. 13th Cambridge Workshop on Cool Stars, Stellar Systems, and the Sun, eds. F. Favata et al., ESA SP-560, 411

Audard, M., Telleschi, A., Güdel, M., Skinner, S.L., Pallavicini, R., & Mitra-Kraev, U. 2004, ApJ, 617, 531

Bertout, C., Robichon, N., & Arenou, F. 1999, A&A, 352, 574

Brickhouse, N.S., Cranmer, S.R., Dupree, A.K., Luna, G.J.M., & Wolk, S. 2010, ApJ, 710, 1835

Calvet, N., Muzerolle, J., Briceño, C., Hernández, J., Hartmann, L., Saucedo, J.L., & Gordon, K.D. 2004, AJ, 128, 1294

Carrasco-González, C., Rodriguez, L.F., Anglada, G., Martí, J., Torrelles, J.M., & Osorio, M. 2010, Science, 330, 1209

Chrysostomou, A., Bacciotti, F., Nisini, B., Ray, T.P., Eislöffel, J., Davis, C.J., & Takami, M. 2008, A&A, 482, 575

Gómez de Castro, A.I. & Verdugo, E. 2007, ApJ, 654, L91

Gopalswamy, N., Aguilar-Rodriguez, E., Yashiro, S., Nunes, S., Kaiser, M.L., & Howard, R.A. 2005, J. Geophys. Res., 110, A12S07

Gorenstein, P., 1975, ApJ, 198, 95

Gosling, J.T., McComas, D.J., Phillips, J.L., Pizzo, V.J., Goldstein, B.E., Forsyth, R.J., & Lepping, R.P. 1995, Geophys. Res. Lett., 22, 1753

Gregory, P.C., & Loredo, T.J., 1992, ApJ, 398, 146

Gregory, P.C., & Loredo, T.J., 1996, ApJ, 473, 1059

Güdel, M., Skinner, S.L., Briggs, K.R., Audard, M., Arzner, K., & Telleschi, A., 2005, ApJ, 626, L53

Güdel, M., Skinner, S.L., Audard, M., Briggs, K., & Cabrit, S. 2008, A&A, 478, 797

Hayashi, M.R., Shibata, K., & Matsumoto, R. 1996, ApJ, 468, L37

Holtzman, J.A., Herbst, W., & Booth, J. 1986, AJ, 92, 1387

Howk, J.C., Cassinelli, J.P., Bjorkman, J.E., & Lamers, H.J.G.L.M. 2000, ApJ, 534, 348

Kastner, J.H., Huenemoerder, D.P., Schulz, N.S., Canizares, C.R., & Weintraub, D.A. 2002, ApJ, 567, 434

Leinert, Ch., Zinnecker, H., Weitzel, N., Christou, J., Ridgway, S.T., Jameson, R., Haas, M., & Lenzen, R. 1993, A&A, 278, 129

Lucy, L.B. 1974, AJ, 79, 745

Petrov, P.P., Zajtseva, G.V., Efimov, Y.S., Duemmler, R., Ilyin, I.V., Tuominen, I., & Shcherbakov, V.A. 1999, A&A, 341, 553

Pott, J.-U., Perrin, M.D., Furlan, E., Ghez, A.M., Herbst, T.M., & Metchev, S. 2010, ApJ, 710, 265

Raga, A.C., Noriega-Crespo, A., & Veláquez, P.F. 2002, ApJ, 576, L149

Richardson, W.H. 1972, J. Opt. Soc. Am., 62, 55

Schegerer, A.A., Wolf, S., Ratzka, Th., & Leinert, Ch. 2008, A&A, 478, 779

St.-Onge, G. & Bastien, P. 2008, ApJ, 674, 1032 (SB08)

Su, Y.-N., Liu, S.-Y., Chen, H.-R., Zhang, Q., & Cesaroni, R. 2007, ApJ, 671, 571

Vuong, M.H., Montmerle, T., Grosso, N., Feigelson, E.D., Verstraete, L., & Ozawa, H. 2003, A&A, 408, 581

Waldron, W.L. & Cassinelli, J.P. 2009, ApJ, 692, L76

Wang, S., Wang, X.Y., Wu, C.S., Li, Y., Chao, J.K., & Yeh, T. 2001, Sol. Phys., 202, 385

Table 1. X-ray Sources Near RY Tau

Object	R.A. (J2000)	Decl. (J2000)	Net Counts (cts)	E_{50} (keV)	Offset ($''$)	P.A. (deg.)
RY Tau	04 21 57.41[a]	+28 26 35.24[a]	12366 ± 111	2.04	...	...
1	04 21 54.97	+28 27 15.53	4±2[b]	0.50	51.6	321.4
2[c]	04 21 55.93	+28 26 47.55	12±4	2.12	23.1	302.2
3	04 21 58.22	+28 26 19.78	43±7	1.82	18.8	145.3
4	04 22 00.09	+28 26 13.39	5±2	2.56	41.5	121.8
5	04 22 01.11	+28 27 19.68	4±2[b]	0.44	66.0	47.7

Note. — X-ray data are from CCD7 (ACIS chip S3) using events in the 0.3 - 8 keV range inside the 3σ source extraction ellipse. Tabulated quantities are: J2000.0 X-ray position (R.A., Decl.), net counts and net counts error from *wavdetect* (accumulated in a 55766 s exposure, rounded to the nearest integer, background subtracted and PSF-corrected); median photon energy (E_{50}), offset and P.A. (measured east from north) of the source, relative to the RY Tau X-ray position.

[a] The *Chandra* position is offset $0.''24$ south of the *HST* GSC vers. 2.3.2 position of RY Tau (HST J042157.408+282635.48) and $0.''33$ southwest of the 2MASS near-IR position (2MASS J042157.401+282635.55).

[b] Low significance detection.

[c] This X-ray source may be associated with optical emission knot Ha6 listed in Table 2 of SB08. See text (Sec. 4.1).

Table 2. RY Tau Spectral Fits

Parameter	Value
Model	2T *vapec*
Time Interval	post-flare
N_H (10^{21} cm^{-2})	5.5 [4.7 - 6.8]
kT_1 (keV)	0.59 [0.46 - 0.70]
$norm_1$ (10^{-3})	0.39 [0.20 - 0.88]
kT_2 (keV)	4.82 [4.20 - 5.67]
$norm_2$ (10^{-3})	1.14 [1.04 - 1.24]
Abundances	varied[a]
χ^2/dof	285.0/282
χ^2_ν	1.01
F_X (10^{-12} ergs cm^{-2} s^{-1})	1.27 (2.16)
$F_{X,1}$ (10^{-12} ergs cm^{-2} s^{-1})	0.09 (0.39)
$F_{X,2}$ (10^{-12} ergs cm^{-2} s^{-1})	1.18 (1.77)
log L_X (ergs s^{-1})	30.67

Note. — Based on XSPEC (vers. 12.4.0) fits of the background-subtracted ACIS-S spectrum binned to a minimum of 5 counts per bin. The fit was restricted to post-flare data with negligible pileup in the elapsed time range t = 30,000 - 58,627 s (4011 cts). The tabulated parameters are absorption column density (N_H), plasma energy (kT), and XSPEC component normalization (norm). Abundances are referenced to Anders & Grevesse (1989). Square brackets enclose 90% confidence intervals. The total X-ray flux (F_X) and fluxes associated with each model component ($F_{X,i}$) are the absorbed values in the 0.2 - 10 keV range, followed in parentheses by unabsorbed values. The total X-ray luminosity L_X is the unabsorbed value in the 0.2 - 10 keV range and assumes a distance of 134 pc.

[a]All metal abundances with the exception of Si were fixed at 0.25 × their solar values, based on a best-fit global metallicity $Z = 0.25\ Z_\odot$. The silicon abundance was allowed to vary in order to reproduce the strong Si XIII He-like triplet at E = 1.86 keV and converged to Si = 1.6 [1.0 - 2.5] × solar.

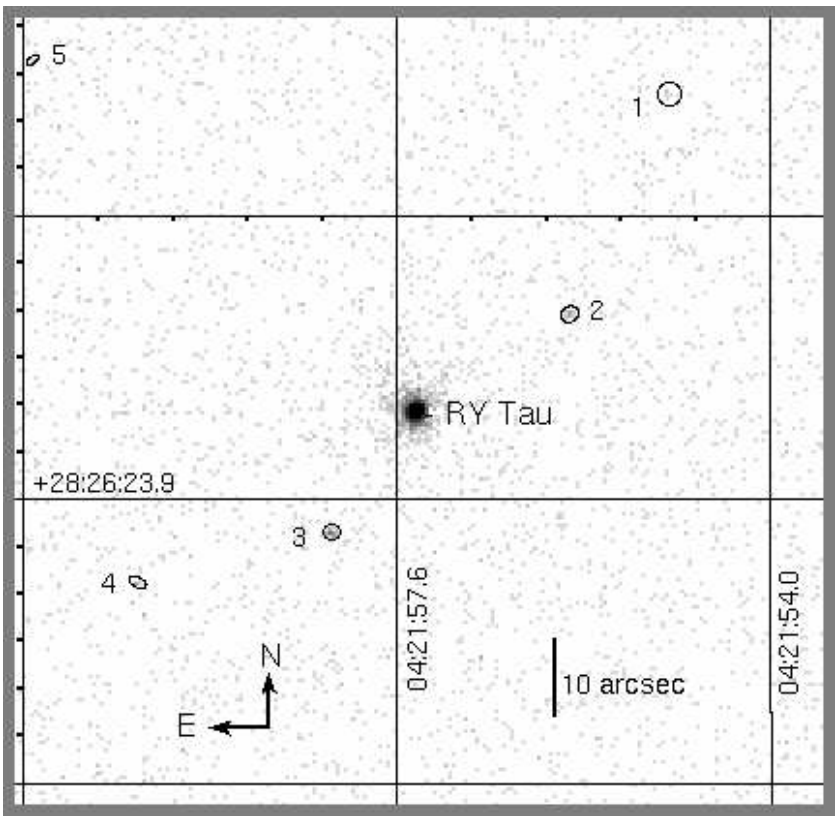

Fig. 1.— Chandra ACIS-S broad-band (0.2 - 8 keV) image of the field near RY Tau. A readout streak running east-west through the center of the image has been removed and filled in with adjacent background. Source numbers refer to Table 1. The X-ray centroid position of RY Tau is J042157.41+282635.24. Pixel size = 0.″492. Log intensity scale.

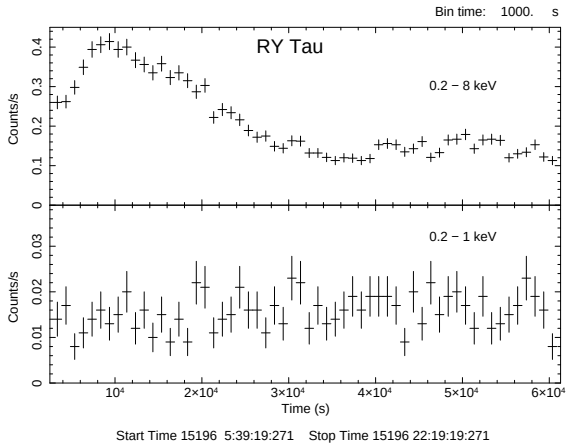

Fig. 2.— Chandra ACIS-S light curves of RY Tau in broad (0.2 - 8 keV) and very-soft (0.2 - 1 keV) bands. The light curves are based on events extracted from a cicular region of radius 3″ centered on the source. The broad-band count rate is slightly underestimated during the flare-peak interval (t = 7000 - 13000 s) due to pileup of ≈10% - 13%. Clear variability is seen in the broad-band light curve but little or no variability is present in the very-soft emission. The binsize is 1000 s. Error bars are 1σ.

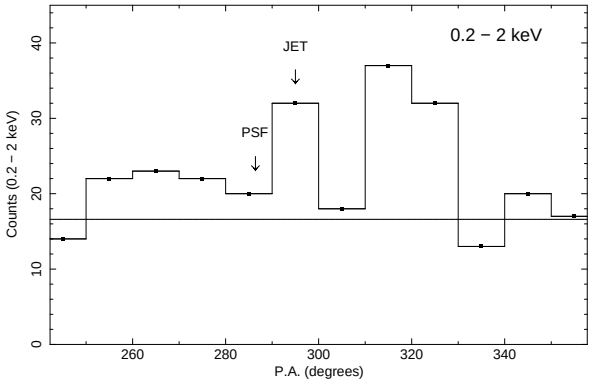

Fig. 3.— Distribution of counts in twelve non-intersecting wedge-shaped regions of equal size near RY Tau as a function of P.A. (measured east from north). The counts were extracted from energy-filtered images (E = 0.2 - 2 keV; no SER or deconvolution applied), using the full exposure time (55.766 ks). Each region has an angular width of 10° and is restricted to a radial range $1'' \leq r \leq 3''$ from the X-ray centroid. The regions are centered at P.A. = 245°, 255°, ... , 355°. The solid horizontal line shows the mean number of counts (mean μ = 16.6, standard deviation $\sigma = 3.5$) computed from all regions of the above size encircling the star. The downward arrows mark the mean P.A. = 295° of the optical jet and the nominal direction of the known PSF asymmetry at P.A. = 286.4°. The PSF asymmetry only produces artificial extension at radii $r \leq 1''$ and thus should not contribute significantly to the counts within radii $r = 1''$ - $3''$ shown in this figure. The strongest excess occurs over the range P.A. = 310° - 320° (5.8σ excess).

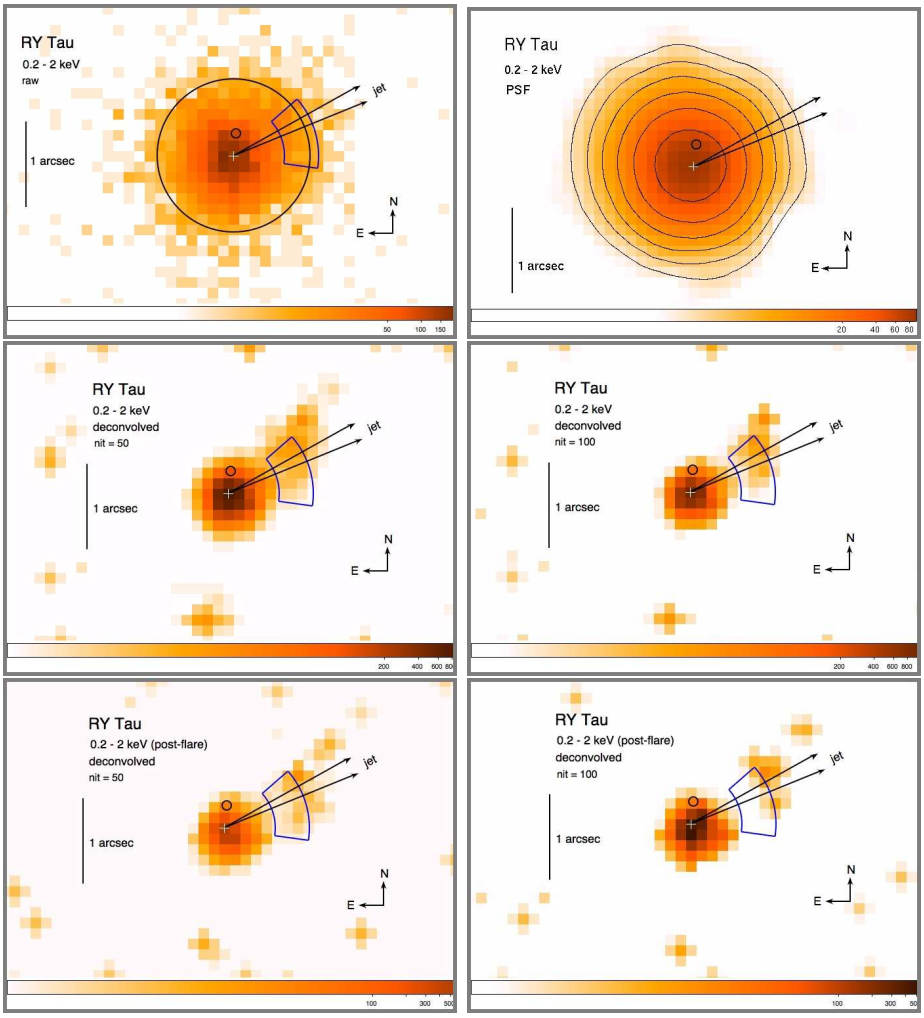

Fig. 4.— Chandra ACIS-S images of RY Tau in the 0.2 - 2 keV band. Log intensity scale; pixel size = 0.″125; pixel randomization removed. The cross (+) at center marks the soft-band X-ray centroid position (J042157.41+282635.22). The small circle marks the *HST* GSC vers. 2.3.2 position of RY Tau (HST J042157.408+282635.48). The vectors of length 1.″7 show the range of directions P.A. = 292° - 299° of the optical jet determined from emission knots (SB08). The roll angle is 268.6° and the focal-plane $+Z$ axis points nearly due west (right). The radially-restricted wedge-shaped region was created using the CIAO tool *make_psf_asymmetry_region* and encloses the area where the known PSF asymmetry can produce artificial structure (P.A. = 286.4° ± 25°; 0.″6 ≤ r ≤ 1.″0). *Top Left*: Raw unsmoothed image using data from the full exposure (6013 events in the 0.2 - 2 keV range). The large circle shows the ACIS 90% encircled power radius R_{90} = 0.″9 (at E ≈ 1 keV). *Top Right*: PSF image used for deconvolution (full exposure) generated using *Chart* and *MARX*. The image has been Gaussian-smoothed using a kernel radius of three pixels. The brightest central pixel contains 94 counts. The inner contour traces the PSF half-maximum, which has a radius of ≈0.″4. The outer contour traces the 1-count level. *Middle*: Deconvolved images from CIAO *arestore* using data from the full exposure with 50 iterations (left) and 100 iterations (right). The images have been lightly Gaussian-smoothed using a kernel radius of one pixel. *Bottom*: Deconvolved images, as above, but restricted to the post-flare time interval (t > 25 ks; 2963 events in the 0.2 - 2 keV range).

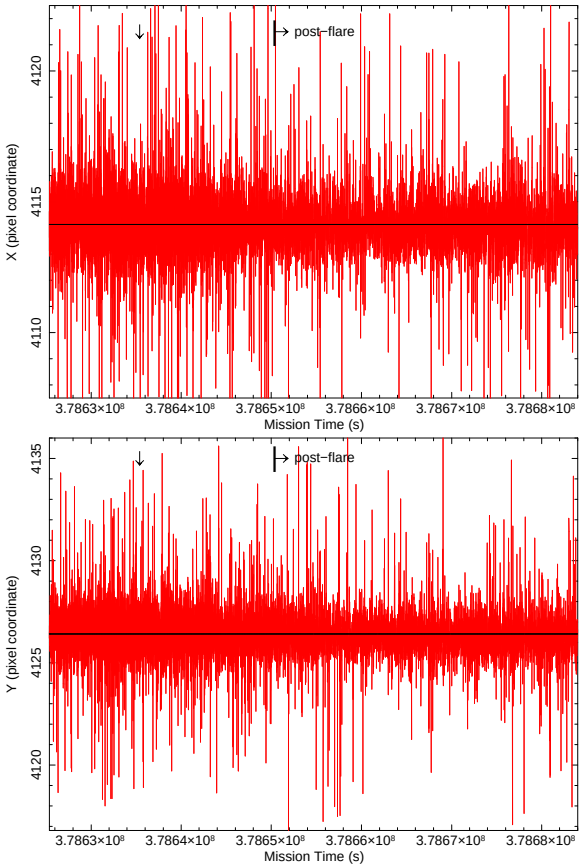

Fig. 5.— Sky-position of RY Tau as a function of mission-time. All events within a radius of 5″ from the X-ray peak are shown. No energy filtering has been applied. The (X,Y) values are sky-pixel coordinates (1 pixel = 0.″492) and correspond to (RA,Dec.) The downward arrow marks the approximate time of flare peak (elapsed time $t = 10$ ks) and the post-flare segment corresponds to $t > 25$ ks. The horizontal line is the mean value. A slightly larger positional scatter is seen during the first 25 ks when the flare occurred.

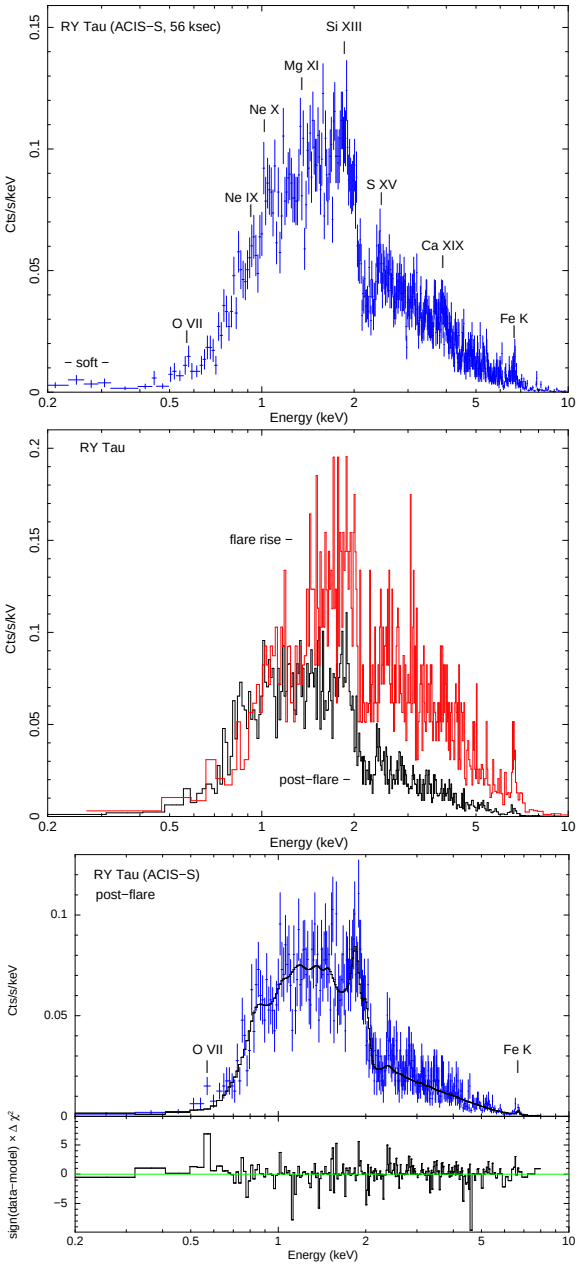

Fig. 6.— *Top*: Chandra ACIS-S spectrum of RY Tau binned to a minimum of 5 counts per bin. The spectrum was extracted from events inside a circular region of radius 3″ centered on RY Tau, and thus includes emission from the star and the extended structure to the northwest (Fig. 4). The spectrum is based on the full exposure (12,504 events), including events recorded during the flare. Faint very-soft emission in the 0.2 - 0.5 keV range is present (48 net counts), some of which likely originates in the the jet or an accretion shock. *Middle*: Same as above, except that the spectra were extracted from specific time intervals corresponding to the flare rise phase (t = 0 - 7 ks) and late post-flare phase (t = 30 ks - 58.6 ks). Error bars omitted for clarity. *Bottom*: Post-flare spectrum overlaid with the best-fit 2T *vapec* model (Table 2). Note that the model does not reproduce the faint O VII emission line, suggesting that this line may be of non-stellar origin (e.g. arising in the shocked jet or an accretion shock).